



Multi-objective optimization of lithium-ion battery model using genetic algorithm approach

Liqiang Zhang^{a,1}, Lixin Wang^a, Gareth Hinds^{b,2}, Chao Lyu^{a,*}, Jun Zheng^a, Junfu Li^a

^a School of Electrical Engineering and Automation, Harbin Institute of Technology, Harbin 150001, China

^b National Physical Laboratory, Teddington, Middlesex TW11 0LW, United Kingdom

HIGHLIGHTS

- Multi-objective genetic algorithm utilized for parameter identification in Li-ion battery model.
- Terminal voltage and surface temperature of the battery are used as optimization objectives.
- Multiple criteria decision making method employed to select the final identification result.
- Model results validated experimentally under a range of operating conditions.

ARTICLE INFO

Article history:

Received 5 February 2014

Received in revised form

16 July 2014

Accepted 17 July 2014

Available online 29 July 2014

Keywords:

Parameter identification

Multi-objective genetic algorithm

Multi-physics model

Lithium-ion battery

ABSTRACT

A multi-objective parameter identification method for modeling of Li-ion battery performance is presented. Terminal voltage and surface temperature curves at 15 °C and 30 °C are used as four identification objectives. The Pareto fronts of two types of Li-ion battery are obtained using the modified multi-objective genetic algorithm NSGA-II and the final identification results are selected using the multiple criteria decision making method TOPSIS. The simulated data using the final identification results are in good agreement with experimental data under a range of operating conditions. The validation results demonstrate that the modified NSGA-II and TOPSIS algorithms can be used as robust and reliable tools for identifying parameters of multi-physics models for many types of Li-ion batteries.

© 2014 Elsevier B.V. All rights reserved.

1. Introduction

In recent years, Lithium-ion batteries have been widely used for electric vehicles and energy storage due to their relatively high energy and power density. A key challenge facing battery manufacturers is the limited durability of the devices under demanding operating conditions. As a result, characterization of battery degradation using material and electrochemical parameters is a popular topic and has attracted many researchers. X. Han et al. [1] and Q. Zhang et al. [2] used the stoichiometric number of the electrode material to indicate the stages of capacity fade. A.P. Schmidt et al. investigated the relationship between the volume

fraction of active material in electrode (ϵ_s), the ionic conductivity of the electrolyte (κ_e) and the cycle number during aging, and used them as characteristics to evaluate the state of health (SOH) of batteries [3]. V. Ramadesigan et al. found that both the electrochemical reaction rate ($k_{s,a}$) and the Li^+ diffusion coefficient ($D_{s,a}$) in the anode degrade with cycle number following a power-law [4]. R. Fu treated some parameters of an electrochemical thermal model as degradation parameters to analyze the degradation effects considering side reactions, including the volume fraction of active material in electrode, the solid electrolyte interface (SEI) resistance (R_{film}) and the diffusion coefficient of electrolyte (D_e) [5]. These papers identified some isolated relationships between a limited number of parameters and battery health. Our research programme, by contrast, is focused on the investigation of a much larger set of model parameters in different stages of aging, which requires an accurate electrochemical model and a nondestructive method for parameter identification.

Several electrochemical models have been presented in the published literature. M. Doyle et al. proposed the P2D model [6,7],

* Corresponding author. P.O. Box 404, Harbin Institute of Technology, No. 92, West Dazhi Street, Nangang District, Harbin 150001, Heilongjiang, PR China. Tel./fax: +86 451 86402965.

E-mail address: lu_chao@hit.edu.cn (C. Lyu).

¹ Electrochemical Society student member.

² Electrochemical Society active member.

which addressed the complex mechanisms of physical and chemical processes such as diffusion, transport of ions, ohmic phenomena and electrochemical reaction, using a group of partial differential equations and some algebraic equations. The Single Particle Model (SPM) has a simpler form and fewer parameters compared to the P2D model; it can predict diffusion and intercalation processes but the local current distribution is neglected, so its use is only valid at low current densities [8]. The Extend-SPM model takes into account the effects of electrolyte concentration and electrochemical reaction distribution [9], but its predictive capability is still inferior to the P2D model. In addition, since thermal behavior is not included in the Extend-SPM model, it is impossible to identify temperature related parameters. The electro-thermal model is a P2D-based model, which includes some thermal behavior such as energy conservation, heat generation and exchange, and can accurately predict a range of phenomena occurring in the battery [10]. P2D-based models have a large set of parameters with corresponding physical meaning, which makes them very suitable for the study of degradation mechanisms. Recently, the experimentally validated simulation results of P2D-based models with accurate parameters have also been used for capacity fading research, such as the degradation behavior caused by Li-plating in low temperature charging process [11] or elementary reaction-based SEI layer generation under different operating conditions [12].

Because of the high complexity and nonlinearity of P2D-based models, analytical solutions do not exist. In addition, the number of parameters is large (27 in this work) so parameter identification is very challenging using conventional approaches. Genetic algorithms (GAs) are a class of stochastic algorithms well-suited for large-scale optimization. They have been successfully applied to parameter identification for equivalent circuit models [13] and P2D models [14] of Lithium-ion batteries. The rationale of the GA procedure is to simulate the process of natural selection and mutation and determine the optimal solution to minimize the errors between simulated data and experimental data.

In previous studies, the constant-current test [4] or the dynamic charge/discharge test [14] at a certain ambient temperature was used for parameter identification. The results are only available for certain identification conditions, while under other conditions (especially at other ambient temperatures) the identified results may not predict the battery performance accurately. The multi-objective optimization approach has been successfully applied to battery modeling by previous authors. P. Kumar et al. [15] used Nondominated sorting Biologically Motivated Genetic Algorithm (NBGA) and J. Brand et al. [16,17] used Nondominated Sorting Genetic Algorithm (NSGA-II) for parameter identification, treating the charge/discharge data at different currents as multi-objectives. Their results demonstrated that this method is applicable to many types of batteries. However, the method has yet to be applied to P2D-based models, and the surface temperature has not been included as an identification objective. In contrast to a traditional genetic algorithm, the multi-objective genetic algorithm provides a set of nondominated solutions instead of a certain optimal solution as an identification result. There remains an uncertainty in the literature over how to decide the final identification result [15–17].

In this article, the parameters of our multi-physics model are identified using a multi-objective genetic algorithm; the remainder of the paper is organized as follows: Section 2 outlines the multi-physics model of a Lithium-ion battery. Section 3 summarizes the experimental setup and test data. Section 4 presents the principle and method of parameter identification using the NSGA-II algorithm. Section 5 provides the final identification result and presents validation studies by comparing the simulated curves with the

experimental data under a range of operating conditions. Conclusions of this article are presented in the final section.

2. Multi-physics model

The multi-physics model consists three parts: the electrochemical model, the thermal model and the radial heat distribution model.

2.1. Electrochemical model

The electrochemical part of the model is described by a conventional P2D model. Fig. 1 shows a schematic of the P2D model for a Lithium-ion battery. It consists of two current collectors, a negative electrode (anode), a separator and a positive electrode (cathode). Both electrodes and separator are porous structures. Two inner boundaries (anode/separator interface 2 and separator/cathode interface 3) and two external boundaries (Cu/anode interface 1 and cathode/Al interface 4) are also shown.

The physical and chemical processes such as ion diffusion and migration and electrochemical kinetics are described by several partial differential equations and algebraic equations in Table 1.

In Eq. (6), E_{ocv} is the equilibrium potential, which is a function of the solid phase Li^+ concentration at the particle surface. The reference E_{ocv} of the graphite/LiFePO₄ system is obtained from Ref. [18], and the reference E_{ocv} of the MCMB/LiCoO₂ system is obtained from Ref. [8]. The meanings of the symbols are explained in detail at the end of this article.

2.2. Thermal model

Thermal phenomena such as energy conservation, heat generation and exchange also occur during the charge/discharge process, and they can be simulated by the P2D model, as presented in Table 2. The heat generation occurs in the spiral roll, including the heat of electrochemical reaction, entropic heat and ohmic heating. Heat exchange, including convection and radiation, only occurs at the surface of the cylindrical battery.

Some parameters in the P2D model, such as solid phase diffusion coefficients $D_{s,a}$ and $D_{s,c}$, solution phase conductivity κ_e , solution phase diffusion coefficient D_e and electrochemical reaction rate $k_{s,a}$ and $k_{s,c}$, are coupled with the battery temperature. These parameters can be updated by the Arrhenius law. In Eq. (15), X_i represents the parameters mentioned above, $X_{i,ref}$ is the parameter

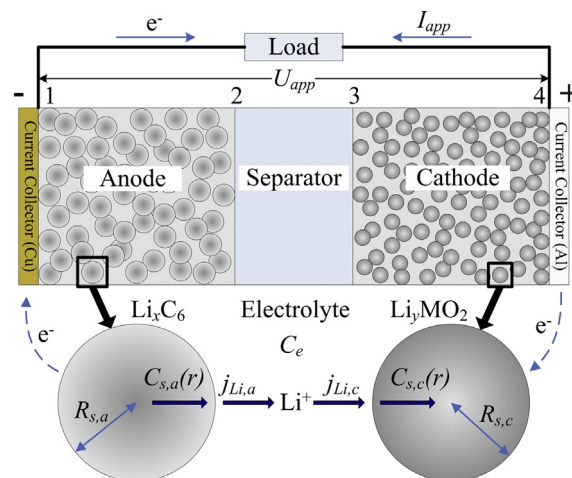


Fig. 1. Schematic of P2D model (discharge process).

Table 1

Governing equations and boundary conditions of the P2D model.

Mechanisms	Equation	Boundary condition
Solid phase diffusion	$\frac{\partial C_s}{\partial t} = \frac{1}{r^2} \nabla \cdot (D_s r^2 \nabla C_s)$	(1) $\left. \frac{\partial C_s}{\partial r} \right _{r=R_0} = -\frac{j_0}{D_s} \left. \frac{\partial C_s}{\partial r} \right _{r=0} = 0$
Electrolyte phase diffusion	$\epsilon_e \frac{\partial C_e}{\partial t} = \nabla \cdot (D_e^{\text{eff}} \nabla C_e) + \frac{a_s}{F} (1 - t_+^0) \cdot i_s$	(2) $\left. \frac{\partial C_e}{\partial x} \right _1 = \left. \frac{\partial C_e}{\partial x} \right _4 = 0, -D_{e,a}^{\text{eff}} \left. \frac{\partial C_e}{\partial x} \right _{2-} = -D_{e,s}^{\text{eff}} \left. \frac{\partial C_e}{\partial x} \right _{2+}, -D_{e,s}^{\text{eff}} \left. \frac{\partial C_e}{\partial x} \right _{3-} = -D_{e,c}^{\text{eff}} \left. \frac{\partial C_e}{\partial x} \right _{3+}$
Solid phase charge balance	$i_1 = -\sigma_s^{\text{eff}} \nabla \phi_s$	(3) $\left. \frac{\partial \phi_s}{\partial x} \right _{2-} = \left. \frac{\partial \phi_s}{\partial x} \right _{3+} = 0, \phi_s _1 = 0, \left. \frac{\partial \phi_s}{\partial x} \right _4 = -\frac{j}{\sigma_{s,a}^{\text{eff}}}$
Electrolyte phase charge balance	$i_2 = -\kappa_e^{\text{eff}} \nabla \phi_e + \frac{2\kappa_e^{\text{eff}} RT}{F} \left(1 + \frac{\partial \ln f_{\pm}}{\partial \ln C_e} \right) (1 - t_+^0) \nabla \ln C_e$	(4) $\left. \frac{\partial \phi_e}{\partial x} \right _1 = \left. \frac{\partial \phi_e}{\partial x} \right _4 = 0, \phi_e _{2-} = \phi_e _{2+}, \phi_e _{3-} = \phi_e _{3+}$
Electrochemical kinetics	$i_s = nFj_{\text{Li}} = i_0 \left[\exp\left(\frac{\alpha_a F}{RT} \eta\right) - \exp\left(-\frac{\alpha_c F}{RT} \eta\right) \right]$	(5)
Overpotential	$\eta = \phi_s - \phi_e - E_{\text{ocv}} - i_s R_{\text{film}}$	(6)
Exchange current density	$i_0 = k_s C_e^{\alpha_a} (C_{s,\text{MAX}} - C_{e/s})^{\alpha_c} C_{e/s}$	(7)
Terminal voltage of the battery	$U_{\text{app}} = \phi_s _4 - \phi_s _1 - iR_{\text{ext}}$	(8)

value at reference temperature T_{ref} , E_i denotes the corresponding activation energy of parameter X_i , respectively. In addition, the equilibrium potential depends on battery temperature according to the Nernst equation (Eq. (16)). An electrochemical–thermal coupled model is presented by feeding back the relationship between temperature dependent parameters and thermal effects to the P2D model. There is a well established literature on the P2D model and the electrochemical–thermal model, the reader is referred to [6–8,18–20] for details.

In Eqs. (11) and (16), dE_{ocv}/dT is the entropy coefficient, and obtained from Ref. [19] for graphite/LiFePO₄ system and Ref. [8] for MCMB/LiCoO₂ system.

2.3. Thermal distribution of cylindrical batteries

A typical cylindrical Li-ion battery is a spiral-rolled cell as shown in Fig. 2. Thin layers of anode, cathode, separator and current collector are stacked up as Section B-B and rolled up on central mandrel as Section A-A, and then inserted into a can. The gaps are filled with liquid electrolyte.

The temperature distribution in the radial direction of a cylindrical battery is more significant than that in the axial direction due to the lower thermal conductivity [21]. For a 26650 type cylindrical battery, the radius is 0.013 m, the heat-transfer coefficient of the lateral surface is $\sim 10\text{--}50 \text{ W m}^{-2} \text{ K}^{-1}$, and the radial thermal conductivity is about $0.15 \text{ W m}^{-1} \text{ K}^{-1}$, so the Biot number is greater than 0.1. The temperature gradient in the radial direction must therefore be taken into account, otherwise the simulated temperature will be very different from the experimental value measured at the surface of the battery [22]. The heat conduction term in Eq. (9) can be expressed in one-dimensional by Fourier's Law:

$$-\nabla(\lambda_r \nabla T) = \lambda_r \left(\frac{\partial^2 T}{\partial R^2} + \frac{1}{R} \frac{\partial T}{\partial R} \right) \quad (17)$$

The temperature gradient at the center of the battery is zero, while at the battery surface it is given by the heat exchange rate at the surface:

$$\begin{cases} \left. \frac{\partial T}{\partial R} \right|_{R=0} = 0 \\ -\lambda_r \left. \frac{\partial T}{\partial R} \right|_{R=R_{\text{cell}}} = \dot{q} \end{cases} \quad (18)$$

where R_{cell} is the radius of the cylindrical battery and the heat exchange rate is \dot{q} is given by $\dot{q} = \dot{q}_c + \dot{q}_r$, where \dot{q}_c and \dot{q}_r are the heat exchange rates due to conduction and radiation respectively. The temperature gradient is continuous at the interfaces of spiral roll, gap and can. The temperature of the can is defined as the shell temperature T_{sh} which can be measured from experiment.

A thermal impedance model has been developed to simulate the thermal distribution in the radial direction of cylindrical Lithium-ion batteries by solving Eq. (17), as detailed in our previous work [23]. In contrast to other studies [14,18,19], the surface temperature is a model output, facilitating its use as an optimization objective in addition to the terminal voltage.

3. Experiments

Two types of Lithium-ion battery are investigated in this article; one is a 2.3 Ah LiFePO₄ battery (A123 system ANR26650m1A, USA), and the other is a 1.8 Ah LiCoO₂ battery (Lishen LS18650BC, China). Before testing, the batteries were charged with standard constant current–constant voltage (CC–CV) strategy – the CC rate was C/3 and the CV voltage was 3.6 V for the LiFePO₄ battery and 4.2 V for the LiCoO₂ battery, and the cutoff current for the CV process was C/50. After a 30 min relaxation, simplified dynamic stress tests (DSTs) were conducted in an environmental chamber (Partner, China) at $T_{\text{am}} = 15^\circ \text{C}$ and $T_{\text{am}} = 30^\circ \text{C}$, respectively. Experimental U_{app} data were acquired by a Battery Testing System (Neware BTS-5V-6A, China) every 10 s, while the experimental T_{sh} data were acquired simultaneously by the auxiliary equipment (Neware BTS-AUX, China) using thermistors as sensors. The temperature sensors were attached to the shell of the batteries using thermally conductive silicone. The simplified DST profiles of these two batteries are shown in Fig. 3.

Table 2
Equations of the thermal model.

Mechanisms	Equation
Energy balance	$\rho C_p \frac{\partial T}{\partial t} = -\nabla \cdot (\lambda \nabla T) + \dot{Q}$ (9)
Electrochemical reaction heat	$\dot{Q}_{\text{rea}} = a_s i_s (\phi_s - \phi_e - E_{\text{ocv}})$ (10)
Entropic heat	$\dot{Q}_{\text{ent}} = a_s i_s T \frac{dE_{\text{ocv}}}{dT}$ (11)
Ohmic heat	$\begin{cases} \dot{Q}_{\text{ohm},s} = \sigma_s^{\text{eff}} \nabla \phi_s \cdot \nabla \phi_s \\ \dot{Q}_{\text{ohm},e} = \kappa_e^{\text{eff}} \nabla \phi_e \cdot \nabla \phi_e + \kappa_e^{\text{D,eff}} \nabla \ln C_e \cdot \nabla \phi_e \\ \dot{Q}_{\text{ext}} = i_{\text{app}}^2 R_{\text{ext}} / L \end{cases}$ (12)
Heat exchange (convection)	$\dot{q}_c = h(T_{\text{sh}} - T_{\text{am}})$ (13)
Heat exchange (radiation)	$\dot{q}_r = \epsilon \sigma (T_{\text{sh}}^4 - T_{\text{am}}^4)$ (14)
Arrhenius' law	$X_i = X_{i,\text{ref}} \exp \left[\frac{E_i}{R} \left(\frac{1}{T_{\text{ref}}} - \frac{1}{T} \right) \right]$ (15)
Nernst equation	$E_{\text{ocv}} = E_{\text{ocv}}^{\text{ref}} + \left(T - T_{\text{ref}} \right) \frac{dE_{\text{ocv}}}{dT}$ (16)

For the LiFePO_4 battery, there are two discharging rates (1C and 2C) and one charging rate (1C) in the test, while for LiCoO_2 , there are three discharging rates (C/4, C/2 and 1C) and two charging rates (C/4 and C/2). There is a trade-off between increasing the number of charge/discharge rates to make the identification result more accurate and robust, at the expense of test complexity and computation time.

4. Parameter identification using multi-objective genetic algorithm

4.1. A modified NSGA-II

The Nondominated Sorting Genetic Algorithm (NSGA-II) is a multi-objective optimization approach first proposed by K. Deb [24]. It provides a set of optimal solutions known as a Pareto front.

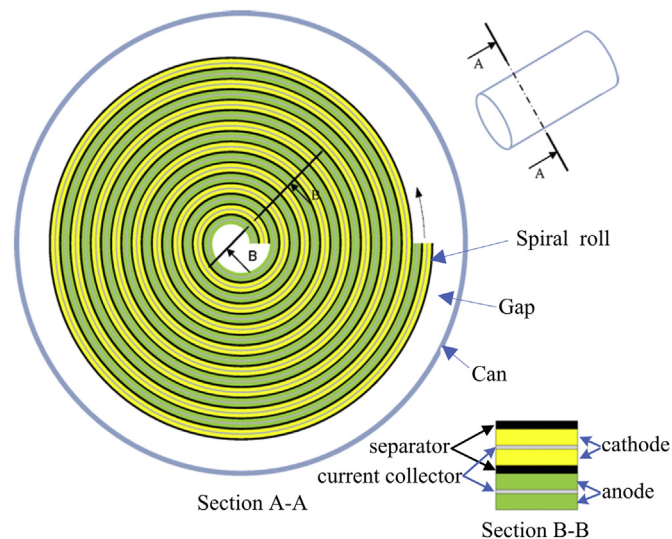


Fig. 2. Cross section of a cylindrical Li-ion battery [20].

The area covered by the Pareto front is called the hyper-volume. Any point inside the hyper-volume is considered to be dominated by at least one solution in the Pareto front. The Pareto front itself is nondominated, means there is no solution in this set that can optimally satisfy all the objectives [16].

In the standard NSGA-II process, a set of parameters is considered to be an individual. Firstly, a population is generated randomly in a certain range; this contains many individuals and is used to calculate the objective functions of each optimization problem. Secondly, the individuals are ranked using a fast nondominated sorting approach according to their objective functions, thus the ranks and crowding-distances are obtained. Thirdly, a binary tournament selection operator is used to choose some better individuals as parents. Fourthly, the parents are crossed-over and mutated to create an intermediate generation. Finally, the new generation is ranked and the process repeats. The Pareto front is obtained by selecting those individuals whose rank value is equal to one. For further background on NSGA-II, the reader is referred to Ref. [24].

Fig. 4 shows the flowchart of the modified NSGA-II. Here we make a slight change to the crossover and mutation process. In the original NSGA-II code [25] these two processes are simple and inefficient. Here we use the real mutation operator and discrete recombination operator in the Genetic Algorithm Toolbox for MATLAB [26] instead of those in the original NSGA-II code. The intermediates generated by these two operators have higher diversity, and the search speed is higher.

The modified NSGA-II has very high universality. It transforms the optimization problems into the objective function, so that the optimization problem is independent of the genetic and non-dominated sorting process. This algorithm is very suitable for solving highly complex and large-scale problems such as parameter identification of a multi-physics model for Lithium-ion batteries.

4.2. Parameter identification

Our previous work [27] has clarified the critical parameters to be identified and their search range. Some of these 25 parameters (such as D_e , R_{film} , etc.) may change their values during the aging process, and therefore the identification result can be used for researching the SOH of a battery. Other parameters (such as k_s , \bar{E} , etc.) must be identified because their values are extremely difficult to measure. In addition, two temperature-related parameters, the average thermal conductivity in the radial direction λ_r , and the heat transfer coefficient h are also included in this analysis. The search ranges of these parameters are shown in Table 4, considering both the benchmark values from references and the probable variation trend during the aging process. For temperature-related parameters, the reference value at the reference temperature (298 K) and the activation energy in the Arrhenius law are both identified. Some Li^+ concentration-related parameters (i.e. D_e and κ_e) are treated as constants here, the reasons being:

- (1) There is no particular formal relationship between the Li^+ concentration and the parameter values; if some universal dependence (e.g. polynomial, exponential or power law) were used, it would incorporate many unknown parameters to be identified, making the identification work more complex or even impossible.
- (2) In Refs. [10,19], particular equations involving electrolyte parameters D_e and κ_e are presented. However, during the aging process, the properties of the electrolyte change significantly, as shown in Refs. [3,5], and these equations no longer represent the real values of those parameters.

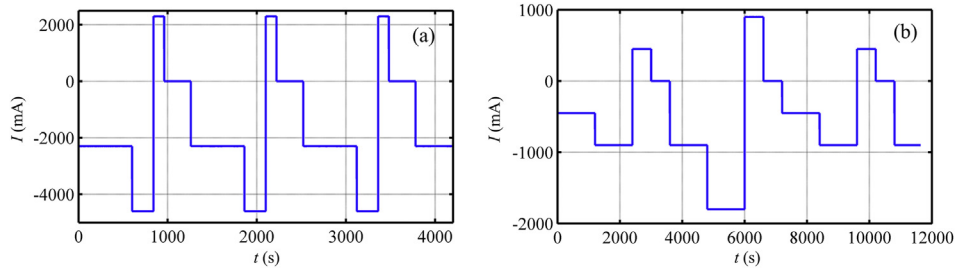


Fig. 3. Current profiles of (a) LiFePO₄ and (b) LiCoO₂ battery in simplified DST.

- (3) From the model simulation we found that the Li⁺ concentration of the electrolyte is relatively constant during the discharging process and has little effect on the parameter values.

As a result, we treated the concentration-related parameters as constants in this paper. In our further work, these parameters will be identified in different aging stages and used for the analysis of electrolyte degradation.

In addition, some geometric parameters (e.g. the thickness of electrode layer) and material properties (e.g. density, specific capacity) are required to complete the model simulation. These parameters have been obtained from battery specifications, literature values or direct measurement after disassembling real batteries.

In this article, the optimal solution of an identification problem is a set of parameters, with which the simulated data should provide a best fit to the experimental data. So, the objective functions

are defined as the Sum of Squares Error (SSE) between the model outputs and the experimental data from the simplified DST at 15 °C and 30 °C. The mathematical formulations are as follows:

$$\text{minimize} \begin{cases} \text{Obj}F_1 = \sum_{i=1}^N (U_{\text{app},i,15^\circ\text{C}} - \hat{U}_{\text{app},i,15^\circ\text{C}})^2 \\ \text{Obj}F_2 = \sum_{i=1}^N (T_{\text{sh},i,15^\circ\text{C}} - \hat{T}_{\text{sh},i,15^\circ\text{C}})^2 \\ \text{Obj}F_3 = \sum_{i=1}^N (U_{\text{app},i,30^\circ\text{C}} - \hat{U}_{\text{app},i,30^\circ\text{C}})^2 \\ \text{Obj}F_4 = \sum_{i=1}^N (T_{\text{sh},i,30^\circ\text{C}} - \hat{T}_{\text{sh},i,30^\circ\text{C}})^2 \end{cases} \quad (19)$$

where $U_{\text{app},i}$ and $T_{\text{sh},i}$ are the model output terminal voltage and surface temperature data, $\hat{U}_{\text{app},i}$ and $\hat{T}_{\text{sh},i}$ are the experimental data, and N is the number of data points.

The objective functions are minimized by using NSGA-II. As these functions approach zero, better agreement is obtained between the model output and the experimental data. The identification code is implemented in MATLAB. We set the population size $NIND = 400$, and the maximum generation $MAXGEN = 200$. Since the simulation time of the simplified DST is about 12 s using the multi-physics model, and the model will be called about 80,000 times during the whole identification, it is computationally expensive and the total time consumption is unacceptable. In order to speed up the identification, we built a computing cluster with 20 cores using an HP ProLiant DL160 G6 server (2 × Intel Xeon L5520 @ 2.26 GHz CPU, 16 GB RAM) and five PCs (Intel Core i3-530 @ 2.93 GHz CPU, 4 GB RAM) based on the MATLAB Distributed Computing Toolbox. The GA identification code was parallelized and successfully accelerated by a factor of over 14 times in our previous work [28]. The same method is used in NSGA-II here, so the actual identification time is about 19 h for each battery.

When the parameter identification is complete, NSGA-II provides a set of optimal solutions called Pareto fronts for each type of battery, instead of a single optimal solution. The individuals on the Pareto front represent different parameter sets, each of them having four objective function values, a rank value and a crowding-distance value. Theoretically, an ideal solution should exist for which all objectives ($\text{Obj}F_1 \sim \text{Obj}F_4$) are minimized. However, by

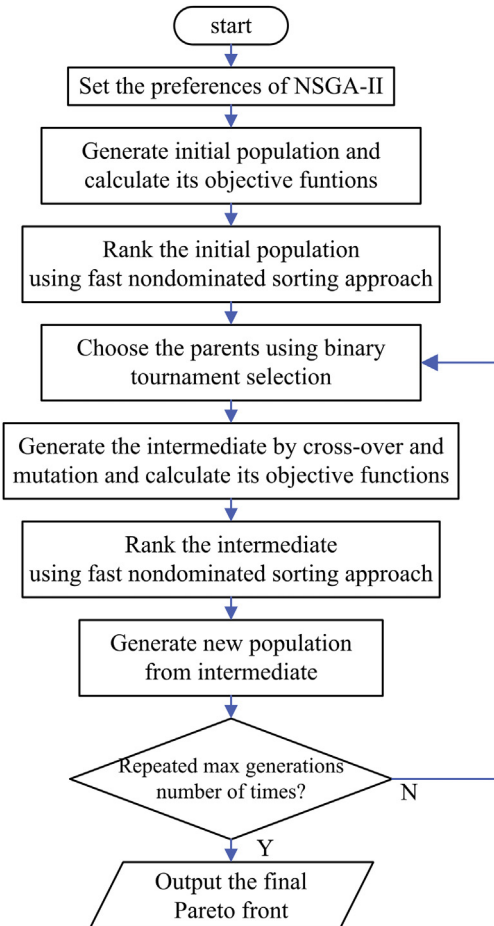


Fig. 4. Flowchart of the modified NSGA-II.

Table 3
Attribute matrix.

Individual	Objective functions			
	F_1	F_2	F_3	F_4
p_1	r_{11}	r_{21}	r_{31}	r_{41}
p_2	r_{12}	r_{22}	r_{32}	r_{42}
...
p_j	r_{1j}	r_{2j}	r_{3j}	r_{4j}
...
p_m	r_{1m}	r_{2m}	r_{3m}	r_{4m}

Table 4

Search range and the final identification results for two types of Li-ion battery.

Parameter	Unit	LiFePO ₄			LiCoO ₂		
		Lower	Upper	Result	Lower	Upper	Result
$R_{s,a}$	(μm)	1	9	1.0247	5	15	7.8502
$R_{s,c}$	(μm)	0.01	0.1	0.0331	5	15	11.2368
$D_{s,a,\text{ref}}$	($\text{m}^2 \text{s}^{-1}$)	5×10^{-15}	1×10^{-13}	9.8910×10^{-14}	1×10^{-14}	9×10^{-14}	6.8814×10^{-14}
$D_{s,c,\text{ref}}$	($\text{m}^2 \text{s}^{-1}$)	5×10^{-19}	1×10^{-17}	4.2958×10^{-18}	5×10^{-15}	5×10^{-14}	1.8062×10^{-14}
$\sigma_{s,c}$	(S m^{-1})	0.1	5	0.4977	1	20	1.1901
x_0	(–)	0.75	0.85	0.7514	0.65	0.78	0.6515
y_0	(–)	0.02	0.08	0.0367	0.4	0.5	0.4347
$\varepsilon_{s,a}$	(–)	0.5	0.6	0.5438	0.3	0.5	0.4319
$\varepsilon_{s,c}$	(–)	0.4	0.6	0.4135	0.4	0.65	0.5610
$R_{\text{film},a}$	(Ωm^2)	0.002	0.01	0.0045	0.001	0.005	0.0002
C_e	(mol m^{-3})	800	1200	1073.6	900	1200	959.6
$D_{e,\text{ref}}$	($\text{m}^2 \text{s}^{-1}$)	1×10^{-11}	1×10^{-9}	3.9378×10^{-11}	2×10^{-10}	1×10^{-9}	2.0241×10^{-10}
$\kappa_{e,\text{ref}}$	(S m^{-1})	0.1	2.5	0.1917	0.2	4	0.2101
R_{ext}	(Ωm^2)	0.002	0.005	0.0031	0.001	0.005	0.0038
$\varepsilon_{e,a}$	(–)	0.3	0.4	0.3442	0.3	0.5	0.3362
$\varepsilon_{e,s}$	(–)	0.4	0.6	0.4068	0.5	0.6	0.5081
$\varepsilon_{e,c}$	(–)	0.3	0.4	0.3015	0.3	0.5	0.3117
$k_{s,a,\text{ref}}$	($\text{m}^{2.5} \text{mol}^{-0.5} \text{s}^{-1}$)	1×10^{-12}	1×10^{-10}	3.9530×10^{-11}	1×10^{-11}	9×10^{-11}	6.9020×10^{-11}
$k_{s,c,\text{ref}}$	($\text{m}^{2.5} \text{mol}^{-0.5} \text{s}^{-1}$)	1×10^{-13}	1×10^{-11}	7.8816×10^{-12}	1×10^{-12}	9×10^{-12}	7.8980×10^{-12}
$\bar{E}k_{s,a}$	(KJ mol^{-1})	10	50	26.81	10	50	39.57
$\bar{E}k_{s,c}$	(KJ mol^{-1})	10	50	31.92	10	50	37.48
$\bar{E}D_{s,a}$	(KJ mol^{-1})	10	50	10.37	10	50	42.77
$\bar{E}D_{s,c}$	(KJ mol^{-1})	10	50	12.86	10	50	18.55
$\bar{E}D_e$	(KJ mol^{-1})	10	50	24.94	5	40	37.04
$\bar{E}k_e$	(KJ mol^{-1})	10	50	41.88	10	50	34.70
A	($\text{W m}^{-1} \text{K}^{-1}$)	0.1	2	0.1517	0.1	3	1.9386
H	($\text{W m}^{-2} \text{K}^{-1}$)	5	50	28.41	5	50	21.45

analyzing the final Pareto front, we found that such an ideal solution does not in fact exist. Solutions on the Pareto front could typically only achieve minimization of one or two objectives and no one solution could optimally satisfy all objectives simultaneously. This means that there is no ideal parameter set with which the simulated data of U_{app} and T_{sh} could perfectly fit the experimental data of the simplified DST at both 15 °C and 30 °C.

However, an optimum solution, which is closest to the ideal solution, should exist on the Pareto front. Therefore, a reasonable and effective method is required to select it from the Pareto front, and this chosen solution will be treated as the final identification result.

4.3. Selection of the final identification result

The purpose of this section is to describe the procedure for selection of a final identification result from each Pareto front using the values of objective functions. The objectives cannot be compared directly because of their different magnitudes and units. This is a typical Multiple Criteria Decision Making (MCDM) problem, for which the Technique for Order Preference by Similarity to Ideal Solution (TOPSIS) [29] can be used to solve it. According to Eq. (19), the ideal solution of the parameter identification problem is the one that can render all four objective functions equal to zero, or failing that equal to minimum values.

In this work, the four values of the objective functions of each individual compose an attribute matrix. For the LiFePO₄ and LiCoO₂ batteries, the Pareto fronts each have 400 solutions. In other words, all individuals in the final population are on the Pareto front, so the dimension of the attribute matrix is (400, 4). As shown in Table 3, p_j ($j = 1, 2, \dots, m$) stands for the j th individual on the Pareto front, $F_i = (r_{i1}, r_{i2}, \dots, r_{im})^T$ ($i = 1, 2, 3, 4$) is the objective function vector of the i th objective, r_{ij} is the i th objective function value of the j th individual, m is the number of individuals in the attribute matrix.

Since the rank values of the individuals in the Pareto front are all the same and equal to 1, this metric is excluded from further study.

Firstly, the attribute matrix is reprocessed according to the crowding-distance. Crowding-distance is used to describe the distance between different individuals in NSGA-II. When the crowding-distance of an individual is equals infinity, it is located on the edge of the Pareto front, and in this case only one objective is minimized. Therefore, the individuals whose crowding-distance are equal to infinity are removed from the attribute matrix.

Secondly, the decision matrix is normalized. It is obvious that each element r'_{ij} in the decision matrix is in the range [0,1], and in the vector F_i the normalized attribute of the optimal individual (which has the minimum objective function value) is 1, while the normalized attribute of the worst individual (which has the maximum objective function value) is 0. The normalization method is:

$$r'_{ij} = \frac{F_i^{\text{MAX}}(p_j) - F_i(p_j)}{F_i^{\text{MAX}}(p_j) - F_i^{\text{MIN}}(p_j)} \quad (20)$$

where F_i^{MAX} and F_i^{MIN} are the maximum and minimum values respectively in vector F_i , and $F_i(p_j) = r_{ij}$ here.

Thirdly, we define an ideal solution $Z^* = (1,1,1,1)$, and a negative ideal solution $Z^- = (0,0,0,0)$. Then the distance between an individual and the ideal solution is obtained as follows, using the Euclidean norm:

$$S_j^* = \sqrt{\sum_{i=1}^4 (Z_{ij} - 1)^2} \quad (j = 1, 2, \dots, m) \quad (21)$$

Similarly, the distance between an individual and the negative ideal solution is:

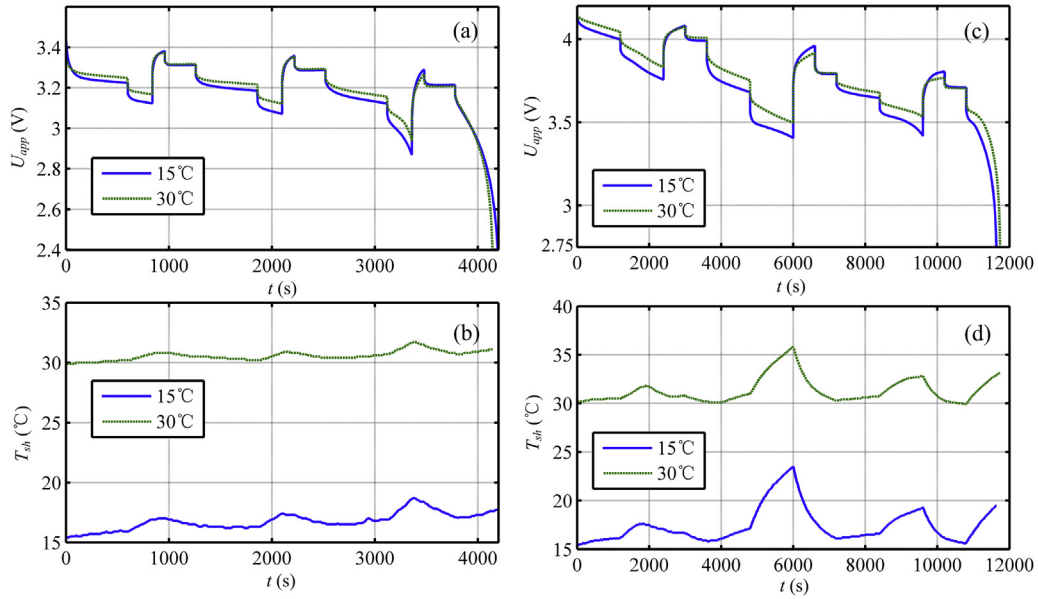


Fig. 5. Experimental data of (a) U_{app} , (b) T_{sh} for LiFePO₄ and (c) U_{app} , (d) T_{sh} for LiCoO₂ battery in simplified DST.

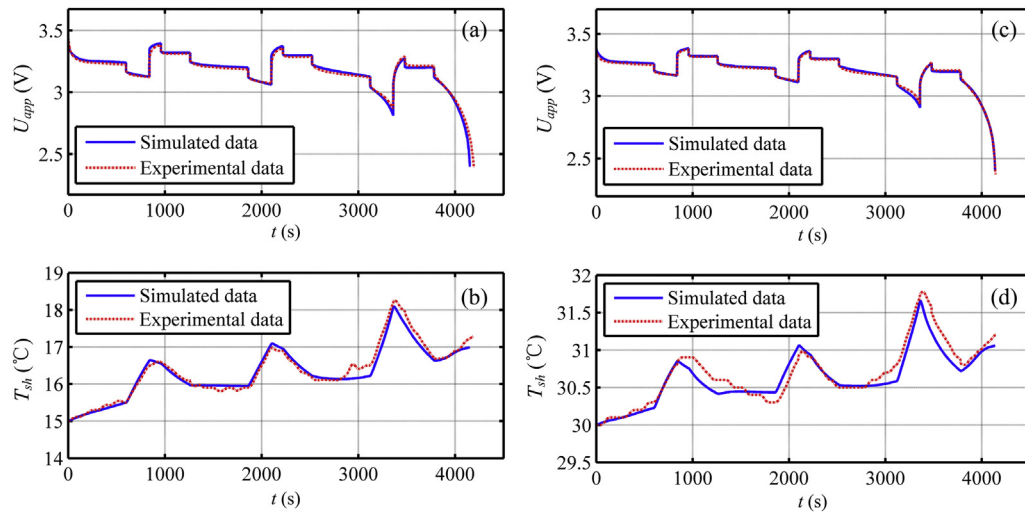


Fig. 6. Comparison of simulated data with experimental data with four identification objectives for the LiFePO₄ battery.

$$S_j^- = \sqrt{\sum_{i=1}^4 (Z_{ij} - 0)^2} \quad (j = 1, 2, \dots, m) \quad (22)$$

where Z_{ij} is the weighted element in the decision matrix:

$$Z_{ij} = W_i r'_{ij} \quad (i = 1, 2, 3, 4 \quad j = 1, 2, \dots, m) \quad (23)$$

where W_i is the weight coefficient of the i th objective. In this work $W = (1, 1, 1, 1)$, which means that the four identification objectives have equal importance in the final decision.

Fourthly, the relative adjacent degree, which is ascertained via the distance between individuals and the ideal solution and the distance between individuals and the negative ideal solution, is obtained as follows:

$$C_j^* = \frac{S_j^-}{S_j^- + S_j^+} \quad (j = 1, 2, \dots, m) \quad (24)$$

where $0 \leq C_j^* \leq 1$. The closer the C_j^* is to 1, the closer an individual is to the ideal solution.

Table 5

Percentile errors and average errors for LiFePO₄ battery parameter identification.

Objectives	Error _{100%}	Error _{75%}	Error _{50%}	Error _{25%}	Error _{avg}
(a) U_{app} at 15 °C	154 mV	16.5 mV	12.9 mV	8.7 mV	14.8 mV
(b) T_{sh} at 15 °C	0.38 °C	0.12 °C	0.07 °C	0.04 °C	0.10 °C
(c) U_{app} at 30 °C	33.6 mV	10.5 mV	8.1 mV	4.9 mV	9.1 mV
(d) T_{sh} at 30 °C	0.34 °C	0.16 °C	0.06 °C	0.02 °C	0.10 °C

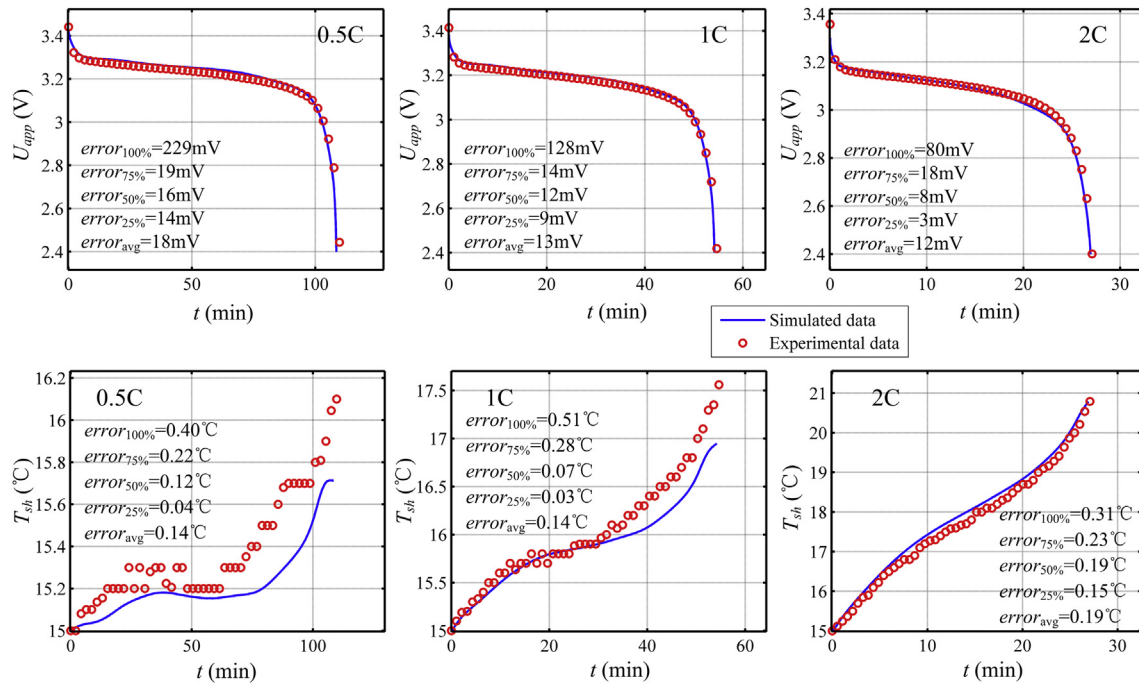


Fig. 7. Discharging characteristics at 0.5C, 1C and 2C for the LiFePO₄ battery at 15 °C.

Finally, all individuals in the attribute matrix are sorted according to the relative adjacent degree. The one that has the maximum C_j^* is the final result of parameter identification.

5. Results and discussion

The variation of potential and surface temperature with time during the DST is shown for each type of battery in Fig. 5. The overpotential of both batteries at 15 °C is greater than that at 30 °C, implying that during the discharge process the terminal voltage at 15 °C is lower, and vice versa during the charging process. This is consistent with a lower diffusion coefficient, lower electrochemical reaction rate and higher internal resistance at the lower temperature. These temperature-related phenomena can be accounted for by the Arrhenius law in the multi-physics model (Eq. (15)). In addition, higher internal resistance also leads to higher heat generation rate, which causes the surface temperature at 15 °C to rise more than that at 30 °C during the discharge process. Traditional single-objective identification uses the U_{app} curve at a certain ambient temperature as the only optimization objective, and therefore the identification results cannot reliably predict temperature-related phenomena at other ambient temperatures. Compared to single-objective identification using only one test, the multi-objective method can provide more accurate and robust results.

Final identification results for the two batteries are listed in Table 4. Significantly, for the 26650-type LiFePO₄ battery, the identified value of λ_r is $0.1517 \text{ W m}^{-1} \text{ K}^{-1}$, which is very close to that ($0.15 \pm 0.01 \text{ W m}^{-1} \text{ K}^{-1}$) measured with a novel experimental technique in Ref. [21]. This demonstrates that the thermal impedance model presented in Section 2.3 is accurate and effective, and that the battery surface temperature is very suitable for identifying thermal parameters. Furthermore, the identified value of h is $20\text{--}30 \text{ W m}^{-2} \text{ K}^{-1}$ for both batteries, much higher than that of free convection air cooling. Forced air convection actually occurs on the battery surface, because the thermal chamber uses flowing air to control the ambient temperature.

The accuracy of the final identification results will be discussed separately for each type of battery in the next two sections. Validation studies are also presented by comparing the simulated and experimental data under several operating conditions.

5.1. LiFePO₄ battery

Fig. 6 compares the simulated data with the experimental data with four identification objectives for the LiFePO₄ battery. All simulated curves agree well with the experimental curves, the percentile errors and average errors are shown in Table 5. Fig. 6(a) and (b) shows the U_{app} and T_{sh} comparison curves at 15 °C, and Fig. 6(c) and (d) shows the U_{app} and T_{sh} comparison curves at 30 °C, respectively.

Discharging tests at several different rates at 15 °C and 30 °C were used to validate the accuracy and robustness of the final identification result. The terminal voltage and surface temperature data are compared with the simulated data in Figs. 7 and 8 respectively. The red (in the web version) marker “○” is experimental data, and the blue solid line is the model simulation using the final identification result. The percentile errors and the average errors between the simulated and experimental data are also shown in each sub-figure.

It is observed that, under all operating conditions, the simulated U_{app} curves fit the experimental data very well, and the average errors in U_{app} never exceed 21 mV for any of the validation conditions. Similarly, the average errors in T_{sh} under all conditions are below 0.19°C . Considering the temperature measurement resolution of our equipment is only 0.1°C , the simulated T_{sh} curves are also in good agreement with the experimental data. This provides confidence in the final identification result and the robustness of the multi-physics model in predicting electrochemical and thermal behavior of real batteries under different operating conditions.

At low rate discharge process, the surface temperature curves present as wave-shape, and the simulated curves seem not well fit to experimental data. Before 70 min at 0.5C discharging, the entropy coefficient of the whole battery changes around zero, leading

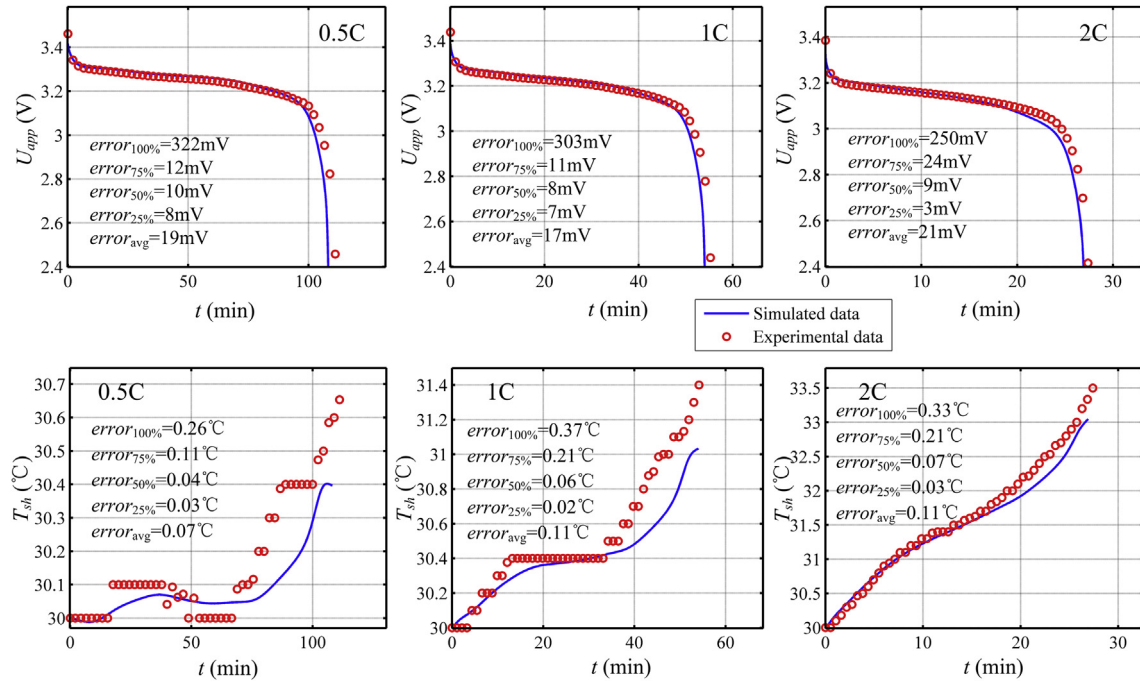


Fig. 8. Discharging characteristics at 0.5C, 1C and 2C for the LiFePO₄ battery at 30 °C.

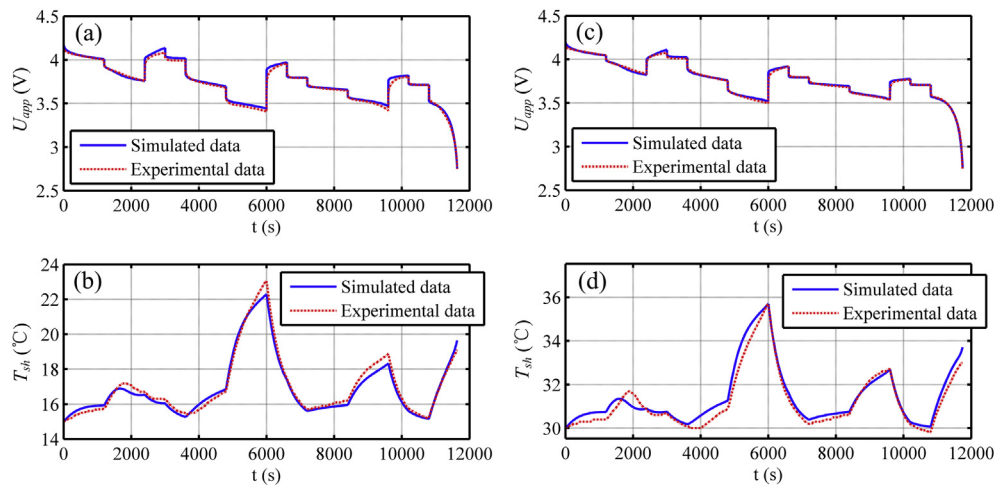


Fig. 9. Comparison of simulated data with experimental data with four identification objectives for the LiCoO₂ battery.

a wave of the surface temperature. And the total temperature rise is only 1.1 °C in Fig. 7 and 0.7 °C in Fig. 8 for 0.5C discharging, compared to the equipment resolution (0.1 °C), the experimental data is actually very rough. But considering the average error is almost equal to the resolution, the relevance between the simulated curves and the experimental data is acceptable. In high rate discharge process, the ohmic heat which is almost constant becomes the main heat generation source and determines the battery's thermal behavior, and the total temperature rise is more than 2 °C, so the T_{sh} curves look more smooth.

5.2. LiCoO₂ battery

Similarly, Fig. 9 compares the simulated data with the experimental data with four identification objectives for the LiCoO₂ battery. Fig. 9(a) and (b) shows the U_{app} and T_{sh} comparison curves at

15 °C, and Fig. 9(c) and (d) shows the U_{app} and T_{sh} comparison curves at 30 °C, respectively. The percentile errors and average errors are given in Table 6. Again, good agreement is observed between simulated and experimental data.

Discharging tests at three different rates (0.5C, 1C and 1.5C) at 15 °C and 30 °C were also used to validate the final identification

Table 6

Percentile errors and average errors for LiCoO₂ battery parameter identification.

Objectives	Error _{100%}	Error _{75%}	Error _{50%}	Error _{25%}	Error _{avg}
(a) U_{app} at 15 °C	136 mV	26.4 mV	12.6 mV	6.2 mV	17.2 mV
(b) T_{sh} at 15 °C	0.78 °C	0.28 °C	0.21 °C	0.11 °C	0.23 °C
(c) U_{app} at 30 °C	76.3 mV	14.3 mV	6.6 mV	3.7 mV	10.0 mV
(d) T_{sh} at 30 °C	0.81 °C	0.39 °C	0.20 °C	0.11 °C	0.26 °C

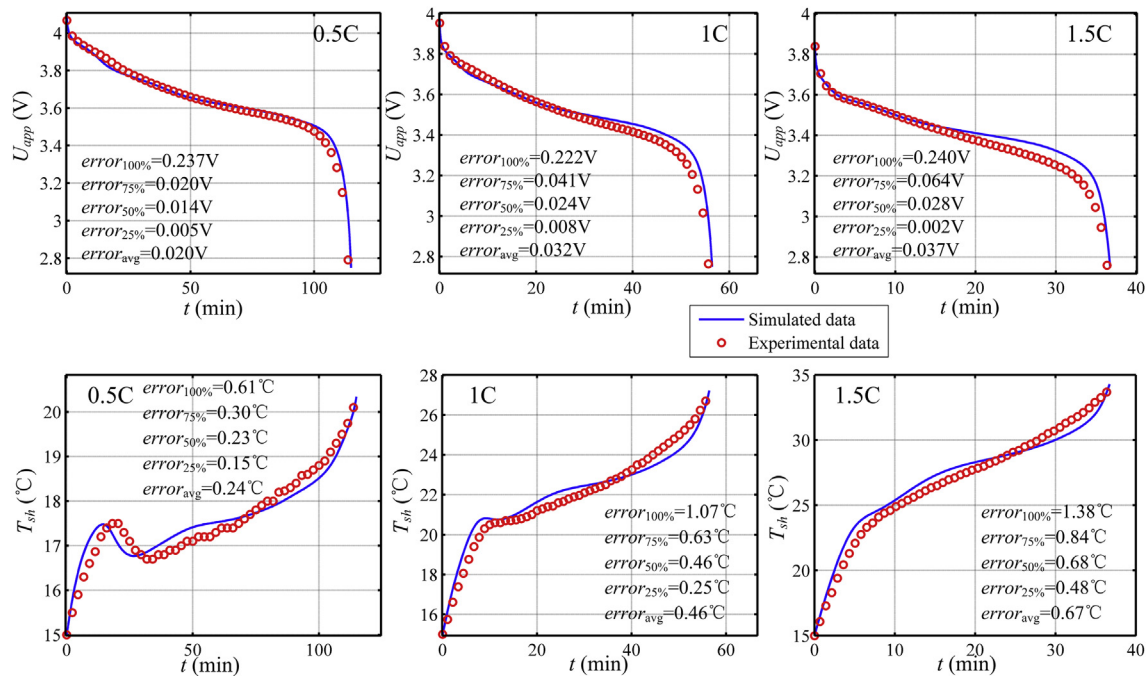


Fig. 10. Discharging characteristics at 0.5C, 1C and 1.5C for the LiCoO₂ battery at 15 °C.

results. Comparisons of simulated and experimental curves are shown in Figs. 10 and 11. At 30 °C, the simulated U_{app} curves fit the experimental data well, and the maximum error never exceeds 64 mV. But at 15 °C, there are some discrepancies between the simulated U_{app} curves and the experimental data during the latter part of the discharge process, leading to a maximum error of over 300 mV at high discharge rates. Since the electrochemical and thermal parts of the model are coupled, an inaccurate voltage output affects the temperature output and vice versa. Both the simulated U_{app} and T_{sh} curves deviate from the experimental data in that period.

The discrepancy is more apparent at higher discharge rates and lower ambient temperature; we speculate that the possible reasons may be: (1) The properties of the active material might be changed under these conditions, and the related parameters no longer constant as assumed in the model. (2) The model ignores some phenomena, such as side reactions. Model simulation cannot predict real battery behavior in these extreme conditions. (3) Some design and geometrical parameters used in the model may be inaccurate. Such parameters are determined by measurement or estimation after disassembling a real LiCoO₂ battery. By contrast, for the LiFePO₄ battery, these parameters are obtained from the literature [18,19], which might imply that they are more accurate and have been experimentally validated by several researchers. (4) The model entropy coefficients and reference equilibrium potential might be different from that in the real battery.

However, the simulated U_{app} and T_{sh} curves with the final identification result capture the major characteristics for all validation data, such as the plateau of terminal voltage and the trend of surface temperature. Though some discrepancies exist in comparison to the LiFePO₄ battery, the correctness and robustness of the final result for the LiCoO₂ battery have been validated.

By the way, the surface temperature evolution of these two types of batteries shows varying behavior under the same operating conditions, because the entropy coefficients of the LiCoO₂ and

LiFePO₄ electrodes are very different. This phenomenon can be used to distinguish the electrode material of a Lithium-ion battery in other applications.

In order to increase the accuracy of parameter identification of the multi-physics model using NSGA-II and TOPSIS method, further work will be carried out on the following aspects:

- (1) Improvements to the accuracy of battery surface temperature would increase the value of surface temperature as an identification objective.
- (2) More accurate values of design or geometrical parameters should be used in model simulation, in order to increase the identifiability of unknown parameters. If such accurate values cannot be obtained directly, they should be identified as unknown parameters.
- (3) More complex operating conditions (i.e. charge/discharge rates and ambient temperatures) should be used as identification tests to increase the robustness of the identification result.
- (4) In the TOPSIS process, a reasonable method for determining the weighting coefficients should be developed based on the credibility of identification objectives. For example, if the accuracy of measured T_{sh} data is relatively low, the objective weight of T_{sh} in Eq. (23) should be lower than that of other credible objectives.

6. Conclusions

In this work, a multi-objective parameter identification method for Lithium-ion batteries using modified NSGA-II and TOPSIS algorithms is proposed. Terminal voltage and surface temperature curves at 15 °C and 30 °C are used as four identification objectives. Two Pareto fronts are obtained using the NSGA-II algorithm for two types of real batteries, and a multiple criteria decision making method TOPSIS is used to select the final identification result from the Pareto front. Simulated data using the final parameter

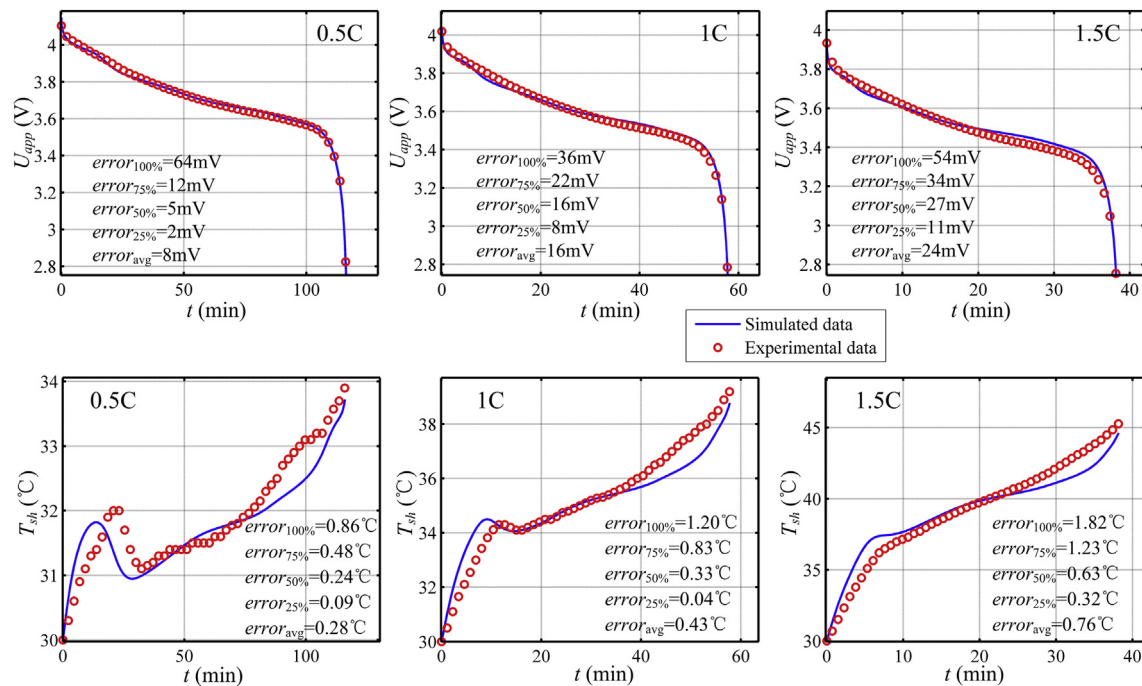


Fig. 11. Discharging characteristics at 0.5C, 1C and 1.5C for the LiCoO₂ battery at 30 °C.

identification results are in good agreement with the experimental data for both types of battery. The identified parameters can indicate the battery's internal characteristics accurately, and can be used for analyzing the aging mechanism in further work. It should be noted that the model outputs with the final results for the LiCoO₂ battery show some discrepancies from the experimental data during the latter part of the discharge process, suggesting that further improvements could be included in the multi-objective parameter identification process.

Acknowledgment

This research was financially supported by the National Natural Science Foundation of China (No. 51107021), and the Fundamental Research Funds for the Central Universities (Grant No. HIT. NSRIF. 2014021).

References

- [1] X. Han, M. Ouyang, L. Lu, J. Li, Y. Zheng, Z. Li, J. Power Sources 251 (2014) 38–54. <http://dx.doi.org/10.1016/j.jpowsour.2013.11.029>.
- [2] Q. Zhang, R.E. White, J. Power Sources 179 (2008) 793–798. <http://dx.doi.org/10.1016/j.jpowsour.2008.01.028>.
- [3] A.P. Schmidt, M. Bitzer, Á.W. Imre, L. Guzzella, J. Power Sources 195 (2010) 7634–7638. <http://dx.doi.org/10.1016/j.jpowsour.2010.06.011>.
- [4] V. Ramadesigan, K. Chen, N.A. Burns, V. Boovaragavan, R.D. Braatz, V.R. Subramanian, J. Electrochem. Soc. 158 (2011) A1048–A1054. <http://dx.doi.org/10.1149/1.3609926>.
- [5] R. Fu, S.Y. Choe, V. Agubra, J. Fergus, J. Power Sources 261 (2014) 120–135. <http://dx.doi.org/10.1016/j.jpowsour.2014.03.045>.
- [6] M. Doyle, T.F. Fuller, J. Newman, J. Electrochem. Soc. 140 (1993) 1526–1533. <http://dx.doi.org/10.1149/1.2221597>.
- [7] M. Doyle, J. Newman, A.S. Gozdz, C.N. Schmutz, J.M. Tarascon, J. Electrochem. Soc. 143 (1996) 1890–1903. <http://dx.doi.org/10.1149/1.1836921>.
- [8] G. Meng, G. Sikha, R.E. White, J. Electrochem. Soc. 158 (2011) A122–A132. <http://dx.doi.org/10.1149/1.3521314>.
- [9] W. Luo, C. Lyu, L. Wang, L. Zhang, J. Power Sources 241 (2013) 295–310. <http://dx.doi.org/10.1016/j.jpowsour.2013.04.129>.
- [10] Y. Ye, Y. Shi, N. Cai, J. Lee, X. He, J. Power Sources 199 (2012) 227–238. <http://dx.doi.org/10.1016/j.jpowsour.2011.10.027>.
- [11] S. Tippmann, D. Walper, L. Balboa, B. Spier, W.G. Bessler, J. Power Sources 252 (2014) 305–316. <http://dx.doi.org/10.1016/j.jpowsour.2013.12.022>.
- [12] Y. Xie, J. Li, C. Yuan, J. Power Sources 248 (2014) 172–179. <http://dx.doi.org/10.1016/j.jpowsour.2013.09.059>.
- [13] Y. Hu, S. Yurkovich, Y. Guezennec, B.J. Yurkovich, Control Eng. Pract. 17 (2009) 1190–1201. <http://dx.doi.org/10.1016/j.conengprac.2009.05.002>.
- [14] J.C. Forman, S.J. Moura, J.L. Stein, H.K. Fathy, J. Power Sources 210 (2012) 263–275. <http://dx.doi.org/10.1016/j.jpowsour.2012.03.009>.
- [15] P. Kumar, P. Bauer, in: Proceeding of: 14th International Power Electronics and Motion Control Conference, 2010, pp. 106–110. <http://dx.doi.org/10.1109/EPEPEMC.2010.5606653>.
- [16] J. Brand, Z. Zhang, R.K. Agarwal, J. Power Sources 247 (2014) 729–737. <http://dx.doi.org/10.1016/j.jpowsour.2013.09.011>.
- [17] A. Malik, Z. Zhang, R.K. Agarwal, J. Power Sources 259 (2014) 76–86. <http://dx.doi.org/10.1016/j.jpowsour.2014.02.062>.
- [18] M. Safari, C. Delacourt, J. Electrochem. Soc. 158 (2011) A562–A571. <http://dx.doi.org/10.1149/1.3567007>.
- [19] Y. Ye, Y. Shi, A.O. Tay, J. Power Sources 217 (2012) 509–518. <http://dx.doi.org/10.1016/j.jpowsour.2012.06.055>.
- [20] X. Zhang, Electrochim. Acta 56 (2011) 1246–1255. <http://dx.doi.org/10.1016/j.electacta.2010.10.054>.
- [21] S.J. Drake, D.A. Wetz, J.K. Ostanek, S.P. Miller, J.M. Heinzel, A. Jain, J. Power Sources 252 (2014) 298–304. <http://dx.doi.org/10.1016/j.jpowsour.2013.11.107>.
- [22] K.E. Thomas, J. Newman, R.M. Darling, Advances in Lithium-ion Batteries, Kluwer Academic Publishers, New York, 2002 (Chapter 12).
- [23] L. Zhang, C. Lyu, G. Hinds, L. Wang, W. Luo, J. Zheng, K. Ma, J. Electrochem. Soc. 161 (2014) A762–A776. <http://dx.doi.org/10.1149/2.048405jes>.
- [24] K. Deb, A. Pratap, S. Agarwal, T. Meyarivan, IEEE Trans. Evol. Comput. 6 (2002) 182–197. <http://dx.doi.org/10.1109/4235.996017>.
- [25] Kanpur Genetic Algorithms Laboratory, <http://www.iitk.ac.in/kangal/codes.shtml> (accessed 03.07.14).
- [26] Complex Optimization and Decision-making Laboratory, <http://codem.group.shef.ac.uk/index.php/ga-toolbox> (accessed 03.07.14).
- [27] L. Zhang, C. Lyu, L. Wang, W. Luo, K. Ma, Chem. Eng. Trans. 33 (2013) 943–948. <http://dx.doi.org/10.3303/CET1333158>.
- [28] L. Zhang, C. Lyu, L. Wang, J. Zheng, W. Luo, K. Ma, Adv. Mech. Eng. 2013 (2013) 1–12. Article ID: 754653, <http://dx.doi.org/10.1155/2013/754653>.
- [29] C.L. Hwang, K. Yoon, Multiple Attributes Decision Making Methods and Applications, Springer, Berlin Heidelberg, 1981.

Nomenclature

C_e : electrolyte concentration (mol m^{-3})
 C_s : concentration of Li⁺ in the intercalation particle (mol m^{-3})

$C_{e/s}$: concentration of Li^+ at the surface of intercalation particle (mol m^{-3})
 D_e : electrolyte diffusion coefficient ($\text{m}^2 \text{s}^{-1}$)
 D_s : Li^+ diffusion coefficient in active material ($\text{m}^2 \text{s}^{-1}$)
 E : activation energy (kJ mol^{-1})
 E_{ocv} : open circuit potential of electrode (V)
 F : Faraday's constant ($=96487 \text{C mol}^{-1}$)
 h : heat transfer coefficient ($\text{W m}^{-2} \text{K}^{-1}$)
 i_{app} : applied current (A)
 i_0 : exchange current density (A m^{-2})
 i_1 : solid phase current density (A m^{-2})
 i_2 : solution phase current density (A m^{-2})
 i_s : electrochemical reaction current density (A m^{-2})
 j_{Li} : wall flux of Li^+ on the intercalation particle of electrode ($\text{mol m}^{-2} \text{s}^{-1}$)
 k_s : electrochemical reaction rate ($\text{m}^{2.5} \text{mol}^{-0.5} \text{s}^{-1}$)
 \dot{q} : heat exchange rate (W m^{-2})
 \dot{Q} : heat generation rate (W m^{-3})
 R : radius of the cylindrical battery (m)
 R_{ext} : contact resistance (Ωm^2)
 R_{film} : SEI film resistance (Ωm^2)
 R_s : intercalation particle radius of electrode (m)
 t_0^+ : Li^+ transference number in the electrolyte
 T : battery temperature (K)
 T_{am} : ambient temperature (K)
 T_{sh} : surface temperature of the battery ($^{\circ}\text{C}$)

U_{app} : applied potential (V)

Greek symbols

α : transfer coefficient of the electrochemical reactions
 ε : emissivity
 ε_s : volume fraction of active material in electrode
 η : overpotential (V)
 κ_e : ionic conductivity of the electrolyte (S m^{-1})
 λ_r : thermal conductivity in the radial direction ($\text{W m}^{-1} \text{K}^{-1}$)
 σ : Stefan–Boltzmann constant ($=5.6704 \times 10^{-8} \text{W m}^{-2} \text{K}^{-4}$)
 σ_s : solid phase conductivity (S m^{-1})
 ϕ_s : solid phase potential (V)
 ϕ_e : solution phase potential (V)

Subscript

a : anode
 c : cathode
 s : separator
 0 : initial value
 ref : reference value